# Capturing Nano-Scale Inhomogeneity of the Electrode Electrolyte Interface in Sodium-Ion Batteries Through Tip-Enhanced Raman Spectroscopy

*Sirshendu Dinda,\* Shivam Trivedi, Ananyo Roy, Frank D. Pammer, and Maximilian Fichtner\**

A prime challenge in the development of new battery chemistries is the fundamental understanding of the generation of the electrode–electrolyte interface (EEI) and its evolution upon cycling. Tip-enhanced Raman spectroscopy (TERS) under an inert gas atmosphere is employed to study the chemical components of the anode/cathode electrolyte interface in a sodium-ion battery. After the first cycle, TERS reveals that the EEI mostly consists of organic carbonate/dicarbonate, oligoethylene oxides, $\alpha,\beta$-unsaturated vinyl ketones/acetates, and inorganic species $ClO_4^-$, $ClO_3^-$, and $Na_2CO_3$. Whereas after $5\times$ cycling, the EEI composition has evolved to contain long chain monodentate or bridging/bidentate carboxylates and alkoxides. The TERS map reveals the nano-scale heterogeneity present in the EEI layers and elucidates a multilayered nano-mosaic coating structure. The sheer volume of Raman signature present in the TERS signal can completely unravel the mysteries regarding the chemical composition and may shed light to the physicochemical behavior of the EEI.

## 1. Introduction

Environmental friendly renewable energy such as solar and wind power faces huge commercial/practical barrier because of their regional and intermittent scarcity. Large-scale energy storage systems (ESSs) are needed to work in sync to overcome this hurdle. Rechargeable batteries are promising candidates for storage

S. Dinda, S. Trivedi, A. Roy, F. D. Pammer, M. Fichtner
Helmholtz Institute Ulm (HIU) Electrochemical Energy Storage
Helmholtzstrasse 11, 89081 Ulm, Germany
E-mail: sirshendu.dinda@kit.edu; m.fichtner@kit.edu
M. Fichtner
Institute of Nanotechnology (INT)
Karlsruhe Institute of Technology (KIT)
Hermann-von-Helmholtz-Platz 1, 76344 Eggenstein-Leopoldshafen, Germany

The ORCID identification number(s) for the author(s) of this article can be found under https://doi.org/10.1002/aenm.202302176

systems as these secondary cells provide practical convenience, long service life, and high efficiency. Sodium-ion batteries (SIBs) are regarded as one of the most usable next-generation ESSs owing to the abundance, and low-cost of sodium. The working principle and required manufacturing methods that are similar to lithium-ion batteries (LIB).[1] In the past decade, tremendous amounts of research have been invested into the development of the active components of SIBs (cathodes, anodes, and electrolytes).[2] Growing demand of sustainability also puts emphasis on the physical properties of EESs, such as long cycling stability, good rate capability, efficient ion transport, and thermal safety.[1c,3] A key property of LIBs that guarantees their stable operation of multiple charge/discharge cycles is the formation of stable electrode–electrolyte interfaces (or interphases) (EEI) at cathode and anode[4]: During electrocycling, both the highly reducing environment at the anode and the oxidizing conditions at the cathode degrade the electrolyte and a composite of the organic and inorganic decomposition products is deposited on the respective electrode surface.[5] The degraded multicomponent materials form a thin EEI interphase on top of cathode/anode and act as an ion-conductive protective mask.[6] The ideal EEI shows high ionic mobility, electronic resistivity, uniform coverage, and interfacial stability.[4,7] It acts as a passivation layer that prevents further electrolyte degradation and enables the sustained cycling stability of the LIBs.[8] A thin and robust solid electrolyte interface (SEI) layer is formed on the surface of the graphite anode in LIBs that resists electron flow to the electrolyte and sustains reversible lithium ion intercalation/extraction in the subsequent cycles. Depending on the electrolyte composition, working conditions, and electrode types, a variety of SEI formations have been observed. To understand the physicochemical nature of the final SEI in LIBs have been modeled as multilayer, mosaic, dual layer, plum-pudding structure, etc.[9] However, despite these extensive efforts, the complex electrochemical reaction mechanisms during the EEI formation are yet to be fully understood.

The situation is even more challenging for the less well-developed SIBs. SIBs suffer from a short cycle life partly attributed to the larger size of sodium ions compared to lithium,

and the associated larger mechanical stress due to larger volume changes induced by (de-) sodiation.[10] The SEI in SIBs is also relatively unstable and continuously evolves during electrochemical cycling.[11] The chemical compositions of the electrolyte in a cell determines the physicochemical nature and passivating quality of the EEIs. The chemical nature of the EEI depends on the composition that regulates the cycling stability of the SIBs. In this regard, fewer works have been directed at understanding the chemical compositions of the SEI or the cathode/electrolyte interface (CEI) in SIBs.

One of the major challenges regarding the characterization of the EEIs is the evolution of the chemical composition during cycling. In literature, the chemical compositions of EEIs in LIBs have been characterized mostly by X-ray photoelectron spectroscopy (XPS), FTIR spectroscopy, NMR spectroscopy, and small-angle neutron scattering (SANS).[12] The applied techniques generally give a rough information of the average chemical components present in the thin EEI layer and provide a basic statement on chemical components. These techniques do not provide any information regarding the heterogeneity or surface distribution of the material, especially in the nanoscale. Indeed, there are very few analytical techniques available that can provide comprehensive chemical information of these thin EEI films. Moreover, some are associated with photon/neutron beam damage, induced in XPS/SANS. Raman spectroscopy is a very powerful nondestructive analytical tool that provides explicit chemical fingerprint but fails to detect thin organic/inorganic SEI layers due to its low cross-section for Raman scattering. Surface-enhanced Raman spectroscopy (SERS) and shell-isolated nanoparticle-enhanced Raman spectroscopy (SHINERS) use plasmon resonance of metal nanostructures to enhance the Raman signal and circumvent the above-mentioned limitation. In LIBs both SERS and SHINERS have been used to elucidate the SEI, but only provide rough chemical information from a diffraction-limited spot on the electrode surface.[13]

Tip-enhanced Raman spectroscopy (TERS) is a highly surface-sensitive method that brings nano-scale spatial resolution and chemical information by coupling scanning probe microscope (SPM) and Raman microscopy.[14] TERS has been used to characterize single molecules bound to atomically smooth metallic surfaces and in ideal cases can detect structural conformers of single molecules.[15] It has been demonstrated that TERS can probe RNA strands and can identify single bases.[16] So far, only a single publication reports the use of TERS to determine nano-scale heterogeneity of the SEI formed during electrochemical cycling on an amorphous silicon surface.[17] In this work, a nanomosaic multilayer SEI structure was identified, consisting of carboxylate and fluorinated species that have been reported as SEI components when lithium hexafluorophosphate (LiPF$_6$, 1 M) in ethylene carbonate (EC) and diethyl carbonate (DEC) 1:1 by volume were used as electrolyte.[17] The study is limited to the anode-electrolyte interface and the amorphous silicon electrode that was prepared by RF magnetron sputtering. This technique provided a relatively smooth surface, far from a practical rough electrode surface. The Raman studies summarized above are all concerned with the study of LIB anodes and cathodes.

In this study, we have used TERS to map the nanoscale chemical heterogeneity of the EEIs of an SIB and attempt to identify its component fragments. The electrodes were prepared manually and the electrochemical cycles were done in a half-cell arrangement using an inorganic electrolyte dissolved in non-aqueous cyclic carbonate solvent. The topography of the EEI and the chemical composition at nanometer lateral resolution are correlated for hard carbon (HC) anode and Prussian blue (PB) cathode in SIB. The gradual evolution of the SEI and the CEI are analyzed after the first and fifth electrochemical cycles in these anode and cathode mediums, keeping the electrolyte same. Furthermore, we used density functional theory (DFT) calculations to calculate Raman spectra of likely SEI components and matched these with the experimental spectra. We found that organic/inorganic carbonate byproducts mixed with carboxylates, and $\alpha,\beta$-unsaturated carbonyl salts are deposited on the electrode surface. Analyzing the TERS mapping we unveil that the EEIs resemble mosaic nano-island structures.

## 2. Results and Discussion

**Figure 1**a shows the schematic of the TERS setup, where a scanning tunneling microscopy (STM) is optically coupled to a Raman microscope. An electrochemically etched gold STM tip ($\approx$30–40 nm tip diameter) captures the morphology of the electrode surface underneath. The STM tip apex acts as a localized surface plasmon source when it reaches to the confocal plane of a 633 nm incident laser beam. Not only that, favorable polarization of the incident light with respect to the tip shank increases the local charge density at the tip apex. This highly localized charge acts as a non-resonant enhancement source named as "lightning rod".[18] The plasmon resonance together with non-resonant "lightning rod" effect greatly enhances the local electromagnetic field and creates a localized "hot spot". The chemical species within the "hot spot" region exhibit enhanced Raman activity and manifest a high signal-to-noise ratio in the far field. Combining STM images with chemical sensitivity from enhanced Raman fingerprint, a collective picture of nanoscale heterogeneity of EEI can be recognized. Though EEI is electronically insulating, electronic structure of the substrate, film thickness, interface between several SEI components, band-bending effects induced by the electric field between tip and sample makes it possible to measure in STM condition. Use of STM-TERS is coming from a versatile, cost-efficient solution to a side illumination geometrical setup. TERS-STM tips are relatively easy to prepare than AFM probes, which brings down the cost of each tip. Metal tips have a high aspect ratio at the tip apex, crucial for the focusing in top and side illumination.[18,19].

To study the anodic EEI, half-cells consisting of an HC-PVDF composite and a sodium metal counter electrode were fabricated and the cells were first discharged to 0.0 V followed by charging until 2.2 V. The discharge curve can be mainly divided into a sloping and a plateau region that corresponds to filling of Na$^+$ ions in graphitic regions of HC followed by pooling into Nanopores.[20] During first discharge, solid electrolyte interphase is formed on the HC surface due to reduction of electrolyte. This is followed by irreversible capacity loss in the first cycle (Figure 1b). The EEI at the cathode has been studied analogously in half cells charged with PB against sodium that were cycled in the 2.0–4.0 V range, first discharge cycle was performed. The charge discharge curve of the PB cathode is presented in Figure 1c. In all cases, 1 M NaClO$_4$ in PC:FEC (98:2 v/v) (propylene carbonate:
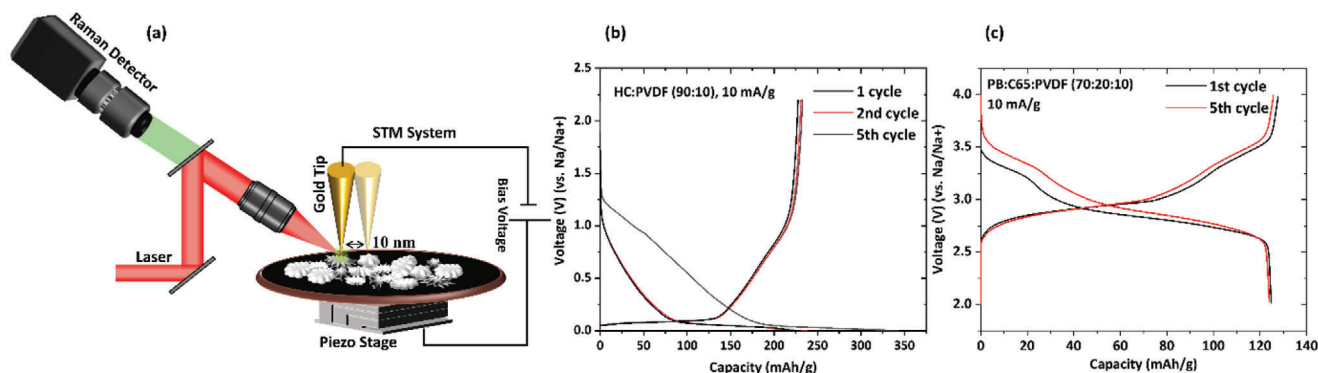
**ADVANCED
SCIENCE NEWS**

www.advancedsciencenews.com

**ADVANCED
ENERGY
MATERIALS**

www.advenergymat.de

**Figure 1.** a) Schematics of the TERS setup. b,c) charge–discharge profile of HC and PB showing 1st and 5th cycle under a constant 10 mA g$^{-1}$ charge/discharge current.

Fluroethylene carbonate) liquid electrolyte has been used. The Raman spectra of the individual carbonate solvent and the combined electrolyte is presented in Figure S1 (Supporting Information).

## 2.1. Solid Electrolyte Interface (SEI) on Hard Carbon Anode

**Figure 2**a shows the STM topography and Figure 2b–e represents TERS mapping of several characteristic Raman bands of the principal components of SEI, present on the hard carbon anode surface after the first electrochemical cycle (1× HC). The topography shows a very rough anode surface that is of the order of few hundreds of nanometers. It is known that peak positions of TERS signals highly depend on the polarization of the electromagnetic field, and hence on the orientation of the polarizing molecules (organic/inorganic fragments) with respect to the excitation field.[21] Thus, the TERS maps have been generated by integrating the area under the curve, rather than relying on the peak intensity (see Figure S2, Supporting Information). The en-

hancement factor of the TERS-STM tip on a malachite green standard sample is ≈6.47 × 10$^6$ (Supporting Information Enhancement Factor Estimation). Due to rapid fading of tip activity, only a fraction of the anode surface is selected and mapped. The TERS maps were generated by considering peaks centered at ≈1140, ≈1370, ≈1481, and lastly 1610 cm$^{-1}$. The vibrational bands corresponding to the mentioned peak positions and their principal components are described in the following sections. The lateral resolution of the TERS image of 1× HC is ≈18–24 nm (see Figure S6, Supporting Information). At a glance, an inhomogeneous distribution of the species can be observed from the TERS map in nanoscale spatial resolution.

The SEI is a heterogeneous complex consisting of inorganic and organic polymeric compounds, formed as a result of electrolyte decomposition.[9e,22] Cyclic carbonate based electrolyte solvents such as PC or FEC undergoes one or multi electron reduction pathways, which leads to the formation of alkyl carbonates, dicarbonates, alkoxides, and oligo-ethylene glycol derivatives through anionic radical intermediates.[23] To analyze the
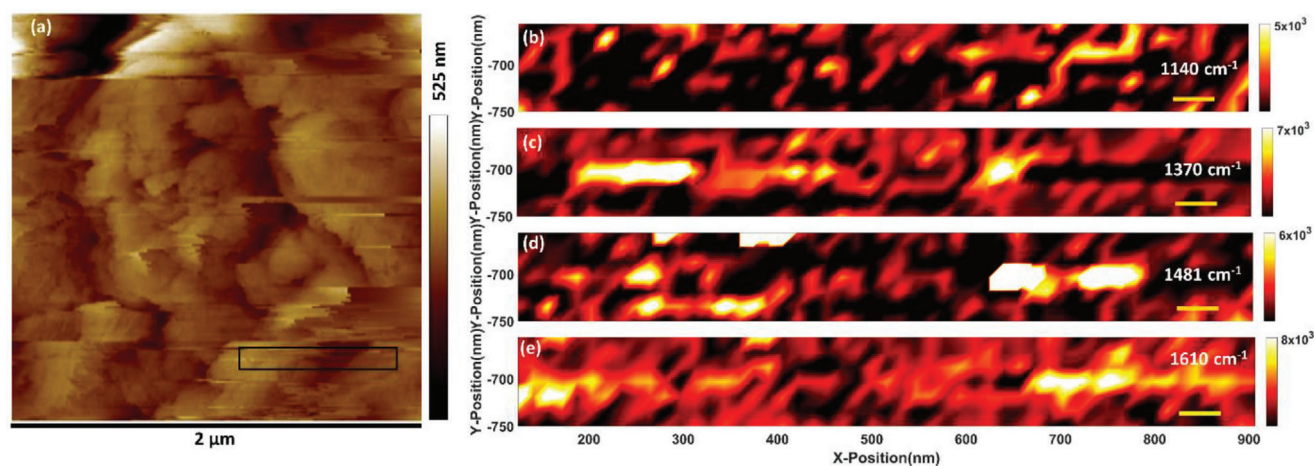


**Figure 2.** a) 2 × 2 µm$^2$ STM topography of the 1× HC. The STM imaging parameters are $I_t$ = 2 nA, $V_b$ = 0.5 V on tip. b) TERS map corresponding to the integration of the [1120–1160] cm$^{-1}$ region with TERS intensity range of 100–5 × 10$^3$ arbitrary units. c) TERS map corresponding to the integration of the [1350–1390] cm$^{-1}$ region with TERS intensity range of 100–7 × 10$^3$ arbitrary units. d) TERS map corresponding to the integration of the [1460–1500] cm$^{-1}$ region with TERS intensity range of 100–6 × 10$^3$ arbitrary units. e) TERS map corresponding to the integration of the [1590–1630] cm$^{-1}$ region with TERS intensity range of 100–8 × 10$^3$ arbitrary units. The scale bars in TERS maps (▬) represent 50 nm spatial length. The details are in the main text.
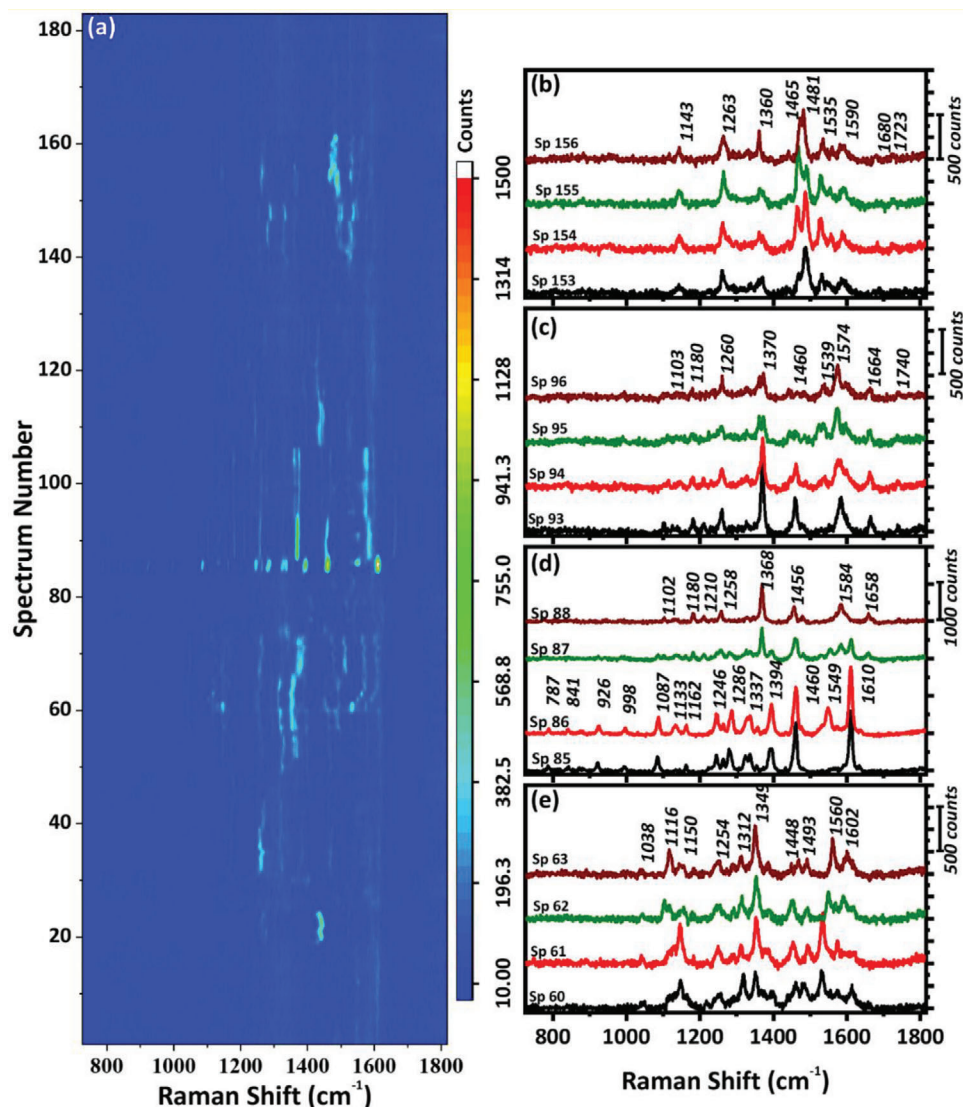
**Figure 3.** a) Waterfall graph of selected TERS spectra of SEI on HC anode after 1× cycle. b–e) comparison plot of TERS spectra collected from various regions of the TERS map. The spectra number in all the plots are corresponding to the respective pixel number of the TERS raster scan. The spectral numbers are correlated with (a) and the spectra are taken from pixels separated by ≈10 nm.

fragmented species, some selected TERS spectra are depicted in waterfall plots (**Figure 3**a). While the TERS spectra contain very complex information compacted together, a general pattern can be discerned on close inspection. Most of the TERS spectra contain features in the spectral region between 1000 and 1640 cm$^{-1}$, which represent the Raman fingerprints of different kinds of vibration of organic and inorganic functional groups such as carbonate ($CO_3^{2-}$), chlorate ($ClO_4^-$), carbonyl (C=O), carboxylate (COO$^-$), dicarbonate [(RO—$CO_2^-$)$_2$], etc. In Figure 3b–e, a collection of TERS spectra are shown that were read off pixels of the TERS map that are ≈10 nm apart from each other. Figure 3b depicts a set of spectra wherein the main Raman bands are centered at 1143, 1263, 1360, 1463, 1481, 1535, 1590, 1680, and 1723 cm$^{-1}$. The most intense band is ≈1480 cm$^{-1}$, is assigned to symmetric O—$CO_2$-bond stretching ($v_{sy}^{O-CO_2}$) of alkyl carbon-

ates (RO—$CO_2^-$, RO—CO—OR) that is coupled with a shoulder band ≈1465 cm$^{-1}$, identified as —$CH_2$ bending ($\delta^{-CH_2}$) or —$CH_3$ deformation bending ($\delta^{-CH_3}$).[24] The band near ≈1360 cm$^{-1}$ also attributed to the $v_{sy}^{O-CO_2}$ vibration in combination with $\delta^{-CH_3}$. The Raman bands at ≈1590 and ≈1680 cm$^{-1}$ are signature bands of asymmetric stretching of —COO ($v_{asy}^{-COO}$). The lower frequency signifies the presence of monomeric alkyl carbonates, whereas the higher frequency is the signature band of the dimeric carbonate form.[24a] The peak at ≈1143 cm$^{-1}$ appears due to asymmetric stretching of C—O—C ($v_{asy}^{C-O-C}$) in (poly) alkyl ethers.[25] Alternatively, the Raman band at ≈1263 cm$^{-1}$ may originate from vibrations of C—O—Na-groups ($v_{sy}^{C-O-Na}$) or twisting of —$CH_2$ groups ($t^{-CH_2}$). The data summarized above is strongly indicates the presence of alkyl dicarbonate ([ROCO$_2$Me]$_2$, R = CH$_2$, Me$_2$CCMe$_2$) or their sodium salts ([ROCO$_2$Na]$_2$). The presence of

ADVANCED
SCIENCE NEWS
www.advancedsciencenews.com

ADVANCED
ENERGY
MATERIALS
www.advenergymat.de

$v_{asy}^{C-O-C}$ band also suggests poly-ethylene oxide (PEO) type polymeric chain also present separately or together with dicarbonate group as $MeO_2COROCO_2Me$ ($R=CH_2-O-CH_2$). The spectrum in Figure 3c, shows features quite similar to the one in Figure 3b, although there is a slight frequency shift in some bands. The most intense bands are located at 1370, 1460, and 1574 $cm^{-1}$. The Raman band at 1574 $cm^{-1}$ can be assigned to the $v_{asy}^{-COO}$ vibration, with $Na^+$ coordinated in a monodentate fashion, whereas 1539 $cm^{-1}$ can be assigned to bidentate or bridging coordination of $Na^+$ (see Schematic S1 Supporting Information).[17] The Raman bands centered at $\approx1103$ and 1180 $cm^{-1}$ are linked to symmetric stretching of $C-O-C$ ($v_{sy}^{C-O-C}$) and $C-CO$ ($v_{sy}^{C-CO}$) of PEO like compounds.[25]

Sp 85 and Sp 86 in Figure 3d show highly defined Raman signals with peaks centered at $\approx787$, 841, 926, 998, 1087, 1133, 1162, 1246, 1286, 1337, 1394, 1460, and 1610 $cm^{-1}$. The most intense peak at 1610 $cm^{-1}$ can be associated with the symmetric stretching vibration of a $C=C$ double bond ($v_{sy}^{C=C}$) conjugated with carbonyl group. A Raman peak centered at $\approx1460$ $cm^{-1}$ is assigned to wagging and scissoring motions of $C-H$-bonds in $-OCH_3$-groups ($w^{-OCH_3}$). Based on these observations, the product is estimated to be a vinyl ketone. We have predicted the complete

Raman spectra of multiple solvents and possible decomposition products or EEI components, including several vinyl ketones via DFT calculations (presented under different sections in Supporting Information). The relatively lower frequency bands are originating from combinations of $C-H$-wagging of $CH_3$-groups and $C-O$-stretching of $C-OCH_3$ ($w^{-CH_3} + v^{C-OCH_3}$). Other bands are associated with bending and twisting vibrations of $-CH_3$ connected with different functional groups. Figure 3e shows the TERS signature from both carbonate polymer and vinyl carbonate. The difference in intensity as well as band peak position suggests that the functional groups in each pixel have orientational heterogeneity with respect to the locally enhanced electric field. Presence of several signature bands in TERS spectra from single pixel reveals a mixture of degraded species and the intensity. Depending on the observation discussed above, the degradation pathway of the electrolyte can be postulated which is represented in **Scheme 1**.

The TERS mappings in Figure 2b–e, were generated by considering peaks centered at $\approx1140$ $cm^{-1}$ ($v_{asy}^{C-O-C}$) from PEO like structures, $\approx1370$ $cm^{-1}$ ($v_{sy}^{O-CO_2} + \delta^{=CH_3}$) from carbonate/dicarbonate polymers, $\approx1481$ $cm^{-1}$ ($v_{sy}^{O-CO_2}$) from carbonate salts and lastly 1610 $cm^{-1}$ ($v_{sy}^{C=C}$) from $\alpha,\beta$-unsaturated ketones
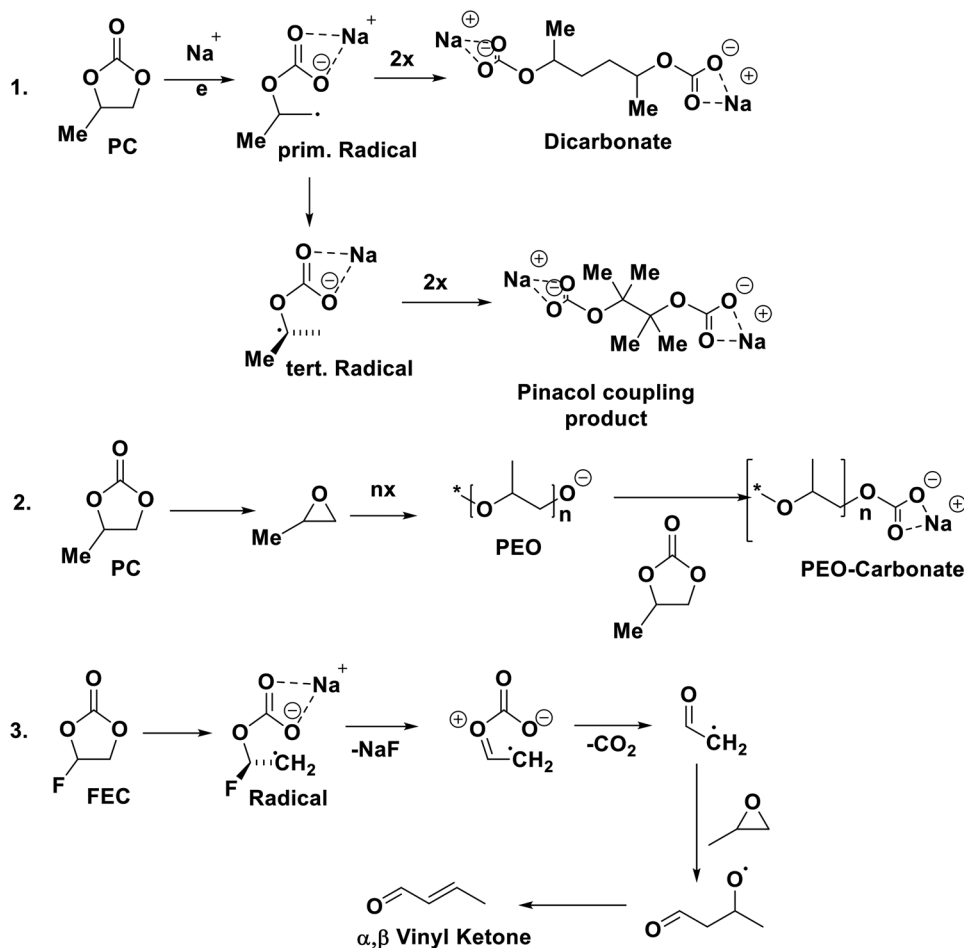


**Scheme 1.** Based on TERS measurements the reduction pathways are hypothesized. The mechanistic way shows the possible pathway for the generation of dicarbonate, PEO-type carbonate, and vinyl ketone-type SEI compounds.[26]
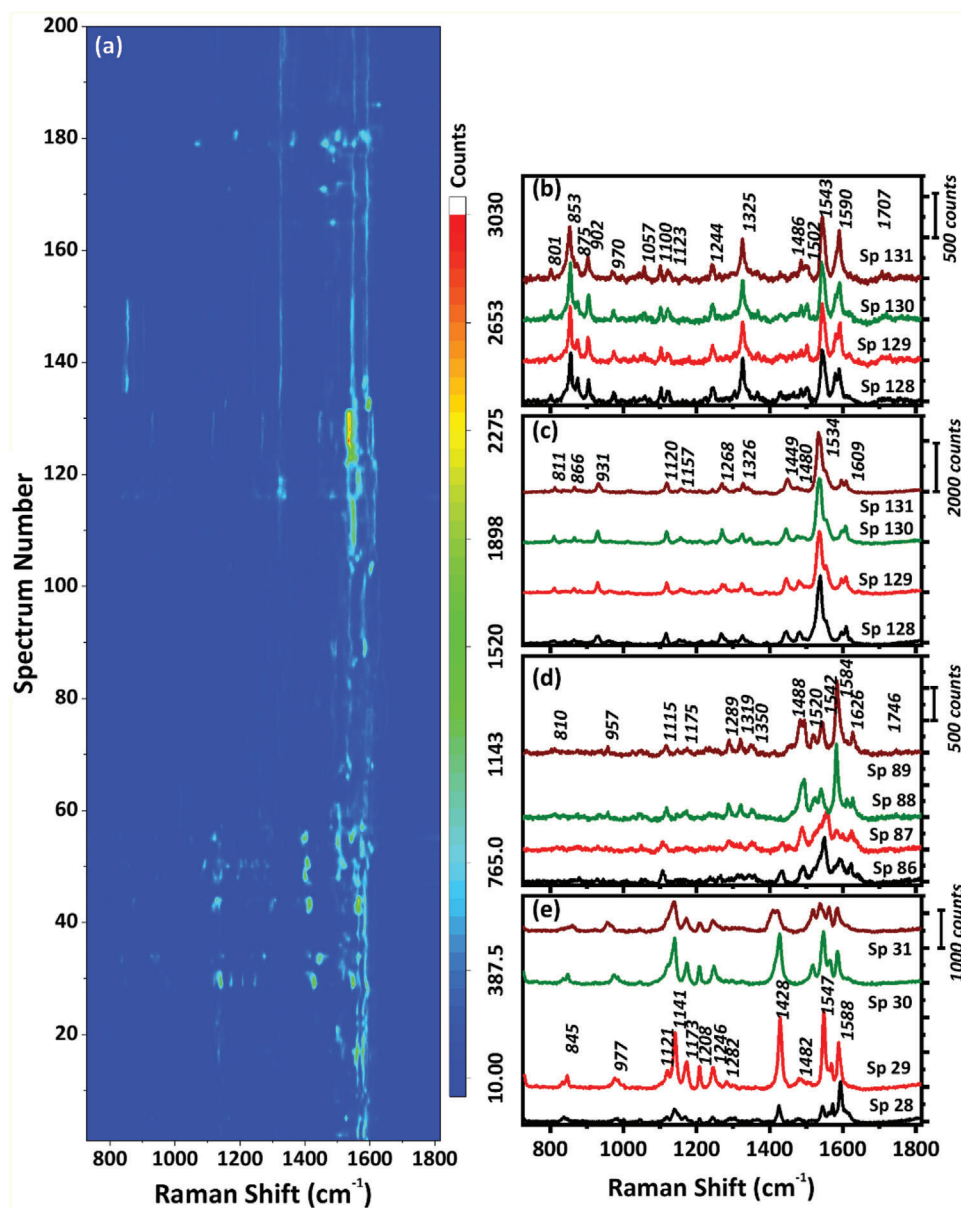
**Figure 4.** a) Waterfall graph of selected TERS spectra of SEI on HC anode after 5× cycle. b–e) comparison plot of TERS spectra collected from various regions of the TERS map. The spectra number in all the plots are corresponding to the respective pixel number of the TERS raster scan.

(vinyl ketones type species). The TERS mapping evidenced that the distribution of the different kinds of organic and inorganic polymers, confirming a high degree of spatial and compositional inhomogeneity of the SEI layer. Although it seems, vinyl ketones are present in high quantity, the band ≈1610 cm$^{-1}$ may also be overlapped by the signature of carbonate vibrations (≈1590–1620 cm$^{-1}$) from monomeric species.

**Figure 4**a presents the waterfall plot of selected TERS spectra from the HC anode surface after the 5th cycle (5× HC). The plot shows structured bands in 1000 to 1640 cm$^{-1}$ region similar to those of 1× HC, whereas a stark contrast is observed in the lower frequency region (<1000 cm$^{-1}$). Relatively high abundance/appearance of low-frequency peaks present in Figure 4(b,c,e) compared to the counterpart of Figure 3(b,c,e)

suggests that similar functional groups are present in the 5× HC SEI but with different polymerization. Several Raman bands with relatively high intensity appear in the low-frequency regions that can be identified in Figure 4b–e. The most intense bands in Figure 4b are 853, 1325, 1543, and 1590 cm$^{-1}$. The high-frequency bands come from symmetric stretching of carboxylates ($v_{sy}^{-COO}$) in monodentate or bridging form. The Raman bands present at ≈853 cm$^{-1}$ are accompanied with several shoulder bands. These signatures are identified as isolated bending vibrations of —CH$_3$ and —CH$_2$ ($\delta^{-CH_3}/\delta^{-CH_2}$) species or skeletal vibrations of C—C chains. —CH$_3$ rocking vibration ($r^{-CH_3}$), and —CH$_2$ wagging vibrations ($w^{-CH_2}$) give rise to 1325 cm$^{-1}$ Raman signature. Several other signatures such as $v^{C-O}$ (≈1050–1100 cm$^{-1}$), $v^{C-CO}$ (≈950–980 cm$^{-1}$), and $v^{CO_3^-}$
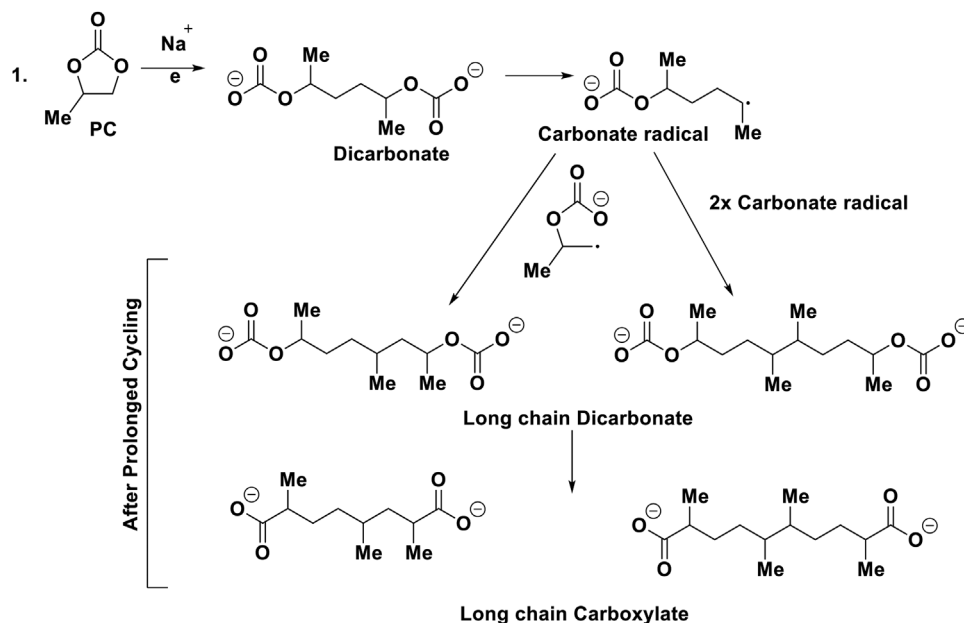
**Scheme 2.** Following the evidence from the TERS in 5× HC, possible formation and degradation pathway of dicarbonate to long-chain carboxylate is presented.

($\approx$870–915 cm$^{-1}$) are also recognizable. The increased intensity of these weak Raman bands emphasizes the presence of long chain hydrocarbons and suggests the formation of polymeric carboxylates and alkoxides in the SEI. TERS band at 1057 cm$^{-1}$ confirms the presence of Na$_2$CO$_3$ species that are formed due to decomposition of organic carbonates.

In Figure 4c, a distinct peak appears at $\approx$931 cm$^{-1}$, which arises from the symmetric stretching of the Cl—O ($v_{sy}^{Cl-O}$) in the chlorate (ClO$_3^-$) species.[27] This can be attributed to the reduction of inorganic perchlorate ion (ClO$_4^-$) to chlorate during prolonged electrochemical cycling.[24b] Surprisingly, TERS spectra do not show significant amounts of ClO$_4^-$ ($\approx$950 cm$^{-1}$) in the SEI layer both in 1× HC and 5× HC anode. Figure 4e represents a group of highly structured TERS spectra in the range $\approx$1100–1300 cm$^{-1}$. Among these, the most intense band ($\approx$1141 cm$^{-1}$) originates from a combination of C—O-stretching of C—ONa-groups and the rocking vibration of —CH$_2$ ($v_{sy}^{C-O} + r^{-CH_2}$).[24a,28] The other Raman bands are associated with different types of —CH$_3$ deformation, —CH$_3$ rocking, —CH$_2$ wagging vibration ($\approx$1173, 1208, 1246, and 1282 cm$^{-1}$) that are present mostly on long chain alkoxide salts.[24a] At the same time, the carboxylate group identifier Raman bands at $\approx$1547 and 1588 cm$^{-1}$ are also present. This suggests, that prolonged electrochemical cycling reduces one end of the long-chain bicarbonate to alkoxides and carboxylates that are absent in 1× HC but present in 5× HC (**Scheme 2**).

The STM topographical image of the 5× HC is presented in **Figure 5**a. The TERS maps in Figure 5b–e have been generated by considering $v^{C=O}$ and —CH$_3$ deformation vibration ($\approx$1325 cm$^{-1}$) of long chain carbonate/bicarbonates, —CH$_2$ wagging vibration ($\approx$1428 cm$^{-1}$) of long chain alkoxides, bidentate/bridging ($\approx$1535 cm$^{-1}$) and monodentate ($\approx$1584 cm$^{-1}$) $v_{asy}^{-COO}$ of long chain carboxylate salts. It is clear from the TERS

map, that the SEI is significantly covered with polymeric carbonates, alkoxides and carboxylates. On the other hand, a large portion of the SEI is still composed of monodentate carboxylate, which suggests that the concentration of the reduced products is still low.

Comparing SEI on 1× HC and 5× HC, we notice a stark dissimilarity in the TERS spectra in the region $\approx$1460–1490 cm$^{-1}$ that represents $v_{sy}^{O-CO_2}$ of the dicarbonate groups such as EDCNa$_2$, DEDC/DEDCNa$_2$, EDCD/EDCDNa$_2$ etc. The absence of this band in case of 5× HC suggests that the generation of dicarbonates has been suppressed in PC-FEC solvents. Dicarbonates decompose to Na$_2$CO$_3$ and CO$_2$ thereby imposes destabilizing effects on the SEI.[29] On the other hand, only trace amounts of the Na$_2$CO$_3$ signature where detected on the 5× HC sample, which reveals the dicarbonates are stable under cycling. Obviously, the dicarbonate layers deposited in primary cycle have been effectively covered by shielding layers of polymeric alkoxides and long chain carboxylates in prolonged electrochemical cycling that sheds light to the better cycling stability in PC-FEC based electrolytes. It has been established that addition of FEC mitigates the formation of Na$_2$CO$_3$ and increase the NaF deposition in the top SEI.[30] The Raman band of NaF is out of the detection range this measured TERS, but very low signature of the Na$_2$CO$_3$ supports the above mentioned fact. The vinyl ketone moieties are also absent in the TRES of 5× HC. Instead, long chain carboxylates and alkoxides are the major part of the SEI in 5× HC. Molecular dynamic simulation on SEI generation in presence of FEC reports addition of small amount of FEC favors bridging/dimeric carboxylate whereas excess FEC is detrimental to the dimer formation.[30a] The amount of dimeric/bridging carboxylates ($\approx$1520–1560 cm$^{-1}$) are higher in 5× HC SEI compared to monomeric carboxylates (Figure 4d–e). This also approves the amount of 5%FEC is still

**ADVANCED
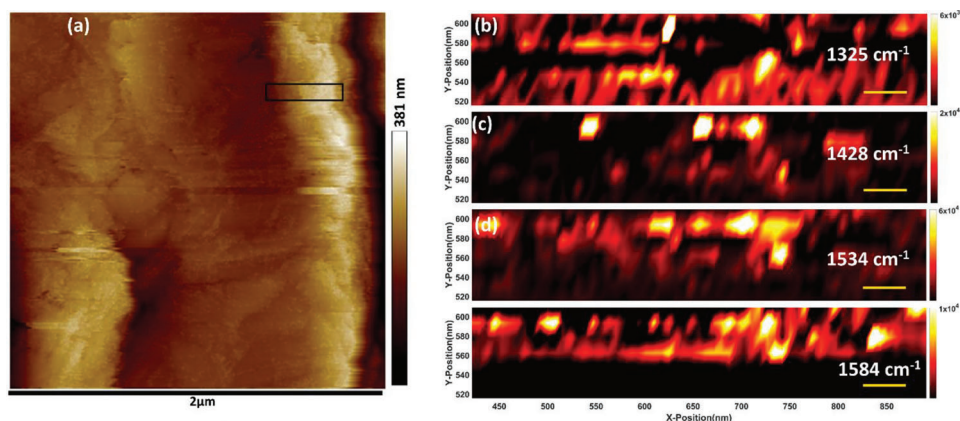SCIENCE NEWS**

www.advancedsciencenews.com

**ADVANCED
ENERGY
MATERIALS**

www.advenergymat.de

**Figure 5.** a) $2 \times 2\ \mu m^2$ STM topography of the 5× HC. The STM imaging parameters are $I_t = 2$ nA, $V_b = 0.5$ V on tip. b) TERS map corresponding to the —CH$_3$ deformation vibration (1325 cm$^{-1}$) with TERS intensity range of 100–6 × 10$^3$ arbitrary units. c) TERS map corresponding to the —CH$_2$ wagging vibration (1428 cm$^{-1}$) with TERS intensity range of 100–2 × 10$^4$ arbitrary units. d) TERS map corresponding to the bidentate/bridging carboxylate vibration (1534 cm$^{-1}$) with TERS intensity range of 100–6 × 10$^4$ arbitrary units. e) TERS map corresponding to the monodentate carboxylate vibration (1584 cm$^{-1}$) with TERS intensity range of 100–1 × 10$^4$ arbitrary units. The scale bars in TERS maps (▬) represent 50 nm spatial length.

under damaging limit where most of the polymeric carboxylate and alkoxide products are bidentate/bridging that are more stable. Thus, the addition of FEC increases coulombic efficiency by stabilizing the SEI.[20b]

### 2.2. Cathode/Electrolyte Interface (CEI) on Prussian Blue Cathode

The TERS spectra from the CEI on 1× PB cathodes are presented in Figure S9 (Supporting Information). The waterfall graph resembles a maze far from well-defined structured graphs of SEI components. This might be coming from huge number of orientational conformers present on the CEI surface. An analysis yields usual Raman signature bands from different functional groups such as $v_{sy}^{CO}$ (≈1620 cm$^{-1}$), $v_{asy}^{-COO}$ (≈1575 cm$^{-1}$), $v_{sy}^{O-CO_2}$ (≈1475 cm$^{-1}$), and $\delta^{-CH_2}$ coupled with twisting of —CH$_2$ (1340 cm$^{-1}$), which can be easily identified. Based on these observations, the organic components of CEI are similar to the SEI counterpart. The usual alkyl carbonate, and alkoxides constitute the major portion of the CEI. Conversely, the observed Raman bands show dense number of peaks at ≈940–960 and ≈1065–1075 cm$^{-1}$ (Figure S9c–e, Supporting Information) with respect to its anode counterpart. The peak centered at ≈955 cm$^{-1}$ is coming from ClO$_4^-$ whereas observed ≈1065 cm$^{-1}$ band is assigned to Na$_2$CO$_3$. Obviously, zeolite water molecules that were removed from PB lattice during cycling reacted with organic carbonate and dicarbonate to form excess Na$_2$CO$_3$.[31] The CEI layer on 1× PB is thus impregnated with larger amount of inorganic substrates that act as an artificial layer that protects the electrode from side effects with the electrolyte. Excellent electronic conduction properties of the inorganic moieties promote rapid charge transfer across the CEI interface.

In Figure S10 (Supporting Information), the waterfall graph of the TERS spectra from the CEI of 5× PB is presented. The TERS spectra are very well structured and defined Raman bands can be found in the higher frequency regions (≈1500–1650 cm$^{-1}$). This indicates a homogeneously oriented organic moieties present on the CEI surface and suggests a relatively smooth CEI surface of

5× PB. Raman bands at high frequency ≈1590–1650 cm$^{-1}$ are coming from $v_{sy}^{CO}$ and $v_{asy}^{CO}$ vibrations, ≈1480cm$^{-1}$ is signature of $v_{sy}^{O-CO_2}$ of carbonate and ≈1156 cm$^{-1}$ is related to $v_{sy}^{C-O} + r^{-CH_2}$ of alkoxide moieties. The absence of low-frequency $\delta^{-CH_3}/\delta^{-CH_2}$ bands or skeletal C—C chain vibrations in the TERS spectra suggest the CEI does not contain long-chain carbonate, alkoxides, or carboxylates that are present in the SEI components of 5× HC. The CEI surface is also devoid of any signature of inorganic Na$_2$CO$_3$ or ClO$_4^-$ species, which again advocate these components are buried under newly formed CEI after 5× cycling.

The topography of 1× PB with the TERS mapping of ClO$_4^-$ (≈948 cm$^{-1}$), PEO (≈1164 cm$^{-1}$), $r^{-CH_3} + w^{-CH_2}$ (≈1340 cm$^{-1}$), and $v_{asy}^{-COO}$ (≈1565cm$^{-1}$) are presented in the Figure S11 (Supporting Information). The TERS map clearly suggests that the CEI surface of the 1× PB is covered with ClO$_4^-$. STM topography alongside with TERS map of 5× PB is reported in Figure S12 (Supporting Information). The TERS map reveals a stark difference from the 5× HC SEI with respect to the relative amount and distribution in the monodentate and bridging carboxylate species. The bridging carboxylates are conglomerated in some specific part with relatively high concentration, conversely monodentate carboxylates (≈1580 cm$^{-1}$) are dispersed heavily on the CEI surface.

## 3. Conclusion

In summary, our results successfully demonstrate that TERS is a very powerful analytical tool that can identify organic and inorganic components of both SEI and CEI of laboratory cells with extremely high chemical sensitivity. The combined effort of STM and TERS mapping provides an excellent topological and chemical view of the EEI surface with very high spatial resolution. In contrast to normal IR or Raman measurements that provide ensemble-averaged information from bulk surface or SHINERS that produce a single point information of EEI, TERS conjure a comprehensive understanding of the spatial distribution and relative abundance (to certain degree) of the EEI components.
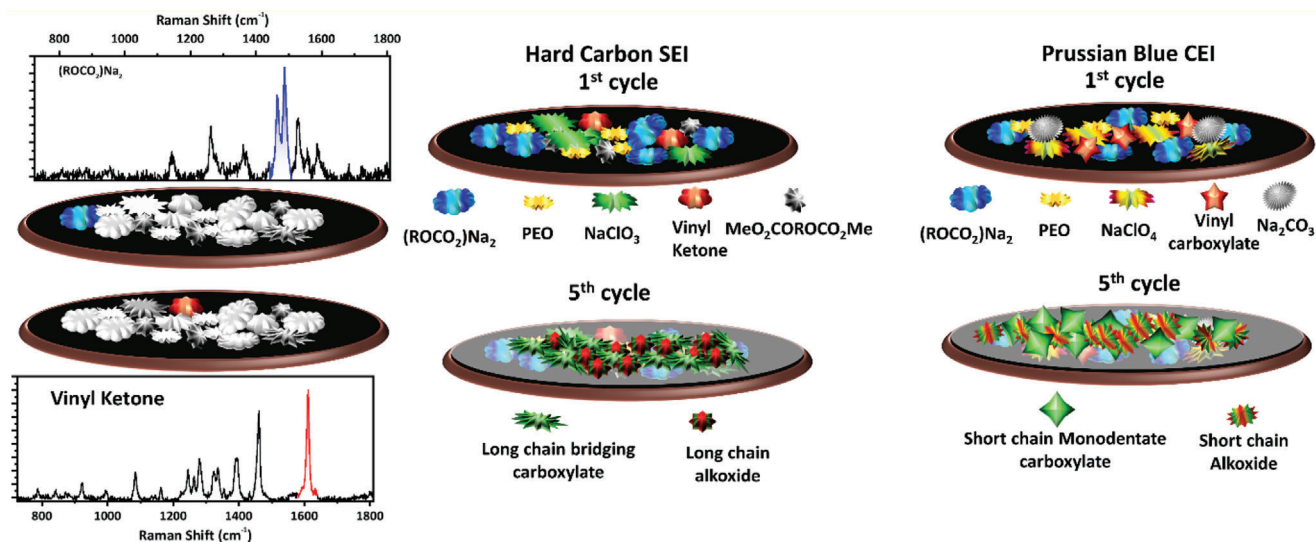
**ADVANCED
SCIENCE NEWS**

www.advancedsciencenews.com

**ADVANCED
ENERGY
MATERIALS**

www.advenergymat.de

**Figure 6.** Illustration of the SEI tomography detection through TERS and its evolution after few cycles. The SEI layer is proposed as nano-mosaic multilayer structure after few cycles.

The TERS study shows the evolution of the different EEI components from 1× to 5×. In primary cycles, mostly alkyl carbonates/bicarbonates, and PEO-like species are present in the EEI surface. In addition, $\alpha$, $\beta$ unsaturated vinyl ketone or $\alpha$, $\beta$ unsaturated vinyl carboxylates are present on the SEI on 1× HC, which are absent in 1× PB CEI surface. Through DFT calculation and comparing TERS data, we have suggested two new EEI species, dicarbonate DEDCNa$_2$ and $\alpha$, $\beta$ unsaturated vinyl carboxylates that are present in the SEI on 1× HC. No inorganic $ClO_4^-$ or $ClO_3^-$ has been found on the 1× HC SEI. Alternatively, CEI on 1× PB cathode contains high amount of $ClO_4^-$ and $Na_2CO_3$ that enables high ionic conductivity in CEI. In subsequent cycling, the SEI components on HC anode further reduced to monodentate/bridging carboxylates or alkoxides with long aliphatic chains. A trace amount of $Na_2CO_3$ and dicarbonate on the SEI suggests suppression of the carbonate formation in presence of FEC. Alternatively, the SEI surface is covered with polymeric bridging carboxylates, which strengthen the EEI layer. On the other hand, CEI on 5× PB is covered mainly with monodentate carboxylates and alkoxides. The TERS map elucidates that both CEI and SEI of SIBs in a half-cell configuration have inhomogeneous, layered, and mosaic-type structures that is illustrated in **Figure 6**. The amount of Raman fingerprint available from the TERS technique makes it tremendously informative analytical technique but untangling individual spectra signature needs more careful and systematical evaluation. TERS is currently the only technique that provides chemical distribution in nano-scale spatial resolution, which can explain mechanistic behavior and physicochemical nature of EEI such as interfacial transport, electrochemical stability, and cycle life.

TERS map generated through areas under different Raman bands shows a nano-heterogeneous distribution, a more robust statistical analysis tool can further evaluate the exact SEI/CEI components. To get a more comprehensive information, hyperspectral analysis tools such as k-mean clustering, PCR-MCA, or manifold clustering have been previously used in different fields of Raman spectroscopy.[17,32] Though our results show an overall integrity of the SEI/CEI components, above mentioned data analysis technique can filter out more precise compositional information.

## 4. Experimental Section

*Sample Preparations of Hard Carbon (HC) Anode*:   HC was synthesized from coconut shell-derived charcoal imported from Vietnam. The charcoal was first ball milled at 400 RPM for 4 h to reduce its grain size. The milled charcoal was then heated at 600 °C for 12 h in an alumina boat. This heating step was followed by another heating step at 1200 °C for 4 h in an argon atmosphere. The furnace was allowed to cool naturally and used as obtained without any washing.

In the first step, a uniform dispersion of PVDF binder in *N*-methyl pyrrolidone (NMP) solvent was obtained by continuous stirring. This dispersion was then added to HC to achieve uniform slurry such that HC:PVDF ratio was 90:10. The slurry was hand-processed and coated on steel current collectors of diameter 1.1 cm. The coated electrodes were dried at 80 °C for 12 h and then at 120 °C for 4 h. The average mass loading was maintained between 1 and 1.5 mg cm$^{-2}$.

*Sample Preparations of Prussian Blue (PB) Cathode*:   Slurry was prepared by mixing active material ($Fe_2(CN)_6$) with carbon super P C65 and PVDF dissolved in NMP in a ratio of 70:20:10. The slurry mixture was stirred overnight and then drop casted on 1.1 cm diameter stainless steel current collector. The casted electrodes were then dried in vacuum for 15 h at 80 °C and then at 120 °C for 4 h.

*Electrochemical Cycling*:   Swagelok-type half cells were assembled in an argon-filled glove box ($O_2$: <0.1 PPM, $H_2O$: <0.1 PPM) using coated electrode as working electrode and sodium metal as the counter electrode. Two borosilicate glass separators (GF/C) dipped in 1 M $NaClO_4$ in PC:FEC 98:2 v/v liquid electrolyte was used as the separating layer between two electrodes. The HC cells were first discharged until 0.0 V followed by charging until 2.2 V at a constant current of 10 mAg$^{-1}$. Keeping the current rate same, PB half cells were also discharged to 2.0 V, then charged up to 4.0 V. These discharge–charge cycles were repeated several times as needed.

The cycled cell was disassembled inside the glove box and the electrode was carefully taken out. The electrode was washed with dimethyl carbonate (DMC) and dried at 60 °C for 30 min. The dried electrode was then examined using TERS.

*TERS Measurements*: TERS instrument is a commercial state-of-the-art spectrometer that combines a RENISHAW inVia Raman microscope with a Bruker nano surface Innova-IRIS scanning probe microscope system through an elongated external optical arm. The optical geometry of the TERS setup is based on side illumination where a long working distance objective (50x, 0.42 NA) is used to focus laser radiation on the tip apex. The excitation and collection efficiency in this geometry is relatively low due to low NA objective and angular collection geometry, but it is necessary to measure opaque of relatively thick surface. The SPM was also placed in a glovebox atmosphere ($O_2$: <0.1 PPM, $H_2O$: 0.0 PPM) that enabled measurements on air/moisture-sensitive EEI surfaces.

In order to established the optical alignments and calibration, STM-TERS measurement was performed on a commercial malachite green sample on gold surface. A gold-etched IRIS STM tip from Bruker was used and 633 nm laser was applied as electromagnetic excitation source. The tunneling current was set at 2 nA and the tip was approached to the surface slowly by keeping the tip bias potential at 0.8 V. Once the tip was engaged, the focal point of the laser at the tip was patiently adjusted to reach at the "hot spot". The input average laser power was 0.5 mW, the exposer time was 1 s and a 1600 l mm$^{-1}$ grooved grating was used as a dispersion element. A second stage of TERS signal was also acquired by lowering the bias voltage to 0.4 V and keeping the tunneling current unchanged. Throughout the TERS measurements, the parameters of tip bias 0.5 V and 2 nA tunneling current were kept unchanged.

The TERS data were collected through IRIS software that controls the Renishaw inVia Raman microscope with Bruker Innova SPM. The IRIS software reads any topographical image created through STM/AFM image. A user-defined selected area was scanned by raster scanning and the TERS signal was recorded. The analyzed (background subtraction, cosmic ray removal) and all the TERS maps were created using homebuilt MatLab script (for details see Supporting Information).

*Density Functional Theory (DFT) Calculations*: Quantum chemical calculations were performed on the bwForCluster JUSTUS 2 at the University of Ulm, using release C.01 of the Gaussian 16 program package. The B3LYP functional was used with added empirical dispersion correction (GD3) in combination with the basis set cc-pVQZ, and the solvent model PCM with THF as solvent.[33] All structures were optimized at the same level of theory and were found to be local minima, according to the frequency calculations. Raman spectra were extracted from the frequency calculation using GaussView 6.0.16. Spectra were generated with a peak half-width at half maximum of 4 cm$^{-1}$.

The Raman shifts (wavenumbers) in computed Raman spectra ($\bar{v}_{DFT}$) were corrected ($v_{corr}$) with the following empirical formula:

$$v_{corr} = \bar{v}_{DFT} * e^{(a*\bar{v}_{DFT})} \tag{1}$$

*a*: empirical scaling constant, $-9.52381 \times 10{-6}$ cm$^{-1}$

The correction constant *a* was derived by fitting the computed spectrum of FEC to the corresponding experimental spectrum.

## Supporting Information

Supporting Information is available from the Wiley Online Library or from the author.

## Acknowledgements

## Conflict of Interest

The authors declare no conflict of interest.

## Data Availability Statement

The data that support the findings of this study are available from the corresponding author upon reasonable request.

## Keywords

[1] a) C. Zhao, Q. Wang, Z. Yao, J. Wang, B. Sánchez-Lengeling, F. Ding, X. Qi, Y. Lu, X. Bai, B. Li, H. Li, A. Aspuru-Guzik, X. Huang, C. Delmas, M. Wagemaker, L. Chen, Y.-S. Hu, *Science* **2020**, *370*, 708; b) Y. Cao, M. Li, J. Lu, J. Liu, K. Amine, *Nat. Nanotechnol.* **2019**, *14*, 200; c) J.-M. Tarascon, *Joule* **2020**, *4*, 1616.

[2] a) V. Palomares, P. Serras, I. Villaluenga, K. B. Hueso, J. Carretero-González, T. Rojo, *Energy Environ. Sci.* **2012**, *5*, 5884; b) H. Kim, H. Kim, Z. Ding, M. H. Lee, K. Lim, G. Yoon, K. Kang, *Adv. Energy Mater.* **2016**, *6*, 1600943; c) N. Yabuuchi, M. Kajiyama, J. Iwatate, H. Nishikawa, S. Hitomi, R. Okuyama, R. Usui, Y. Yamada, S. Komaba, *Nat. Mater.* **2012**, *11*, 512; d) A. Ponrouch, E. Marchante, M. Courty, J.-M. Tarascon, M. R. Palacín, *Energy Environ. Sci.* **2012**, *5*, 8572.

[3] H. S. Hirsh, Y. Li, D. H. S. Tan, M. Zhang, E. Zhao, Y. S. Meng, *Adv. Energy Mater.* **2020**, *10*, 2001274.

[4] C. Yan, R. Xu, Y. Xiao, J.-F. Ding, L. Xu, B.-Q. Li, J.-Q. Huang, *Adv. Funct. Mater.* **2020**, *30*, 1909887.

[5] W. Cai, Y.-X. Yao, G.-L. Zhu, C. Yan, L.-L. Jiang, C. He, J.-Q. Huang, Q. Zhang, *Chem. Soc. Rev.* **2020**, *49*, 3806.

[6] a) K. Xu, *Chem. Rev.* **2004**, *104*, 4303; b) K. Xu, *Chem. Rev.* **2014**, *114*, 11503.

[7] K. Song, W. Chen, *Chem* **2021**, *7*, 3195.

[8] a) J. B. Goodenough, Y. Kim, *Chem. Mater.* **2010**, *22*, 587; b) L. Ma, J. Cui, S. Yao, X. Liu, Y. Luo, X. Shen, J.-K. Kim, *Energy Storage Mater.* **2020**, *27*, 522.

[9] a) K. Kanamura, H. Tamura, S. Shiraishi, Z.-i. Takehara, *J. Electroanal. Chem.* **1995**, *394*, 49; b) E. Peled, D. Golodnitsky, G. Ardel, *J. Electrochem. Soc.* **1997**, *144*, L208; c) S. Shi, P. Lu, Z. Liu, Y. Qi, L. G. Hector Jr., H. Li, S. J. Harris, *J. Am. Chem. Soc.* **2012**, *134*, 15476; d) Y. He, L. Jiang, T. Chen, Y. Xu, H. Jia, R. Yi, D. Xue, M. Song, A. Genc, C. Bouchet-Marquis, L. Pullan, T. Tessner, J. Yoo, X. Li, J.-G. Zhang, S. Zhang, C. Wang, *Nat. Nanotechnol.* **2021**, *16*, 1113; e) J. Zhang, J. Gai, K. Song, W. Chen, *Cell Rep. Phys. Sci.* **2022**, *3*, 100868.

[10] a) N. Yabuuchi, K. Kubota, M. Dahbi, S. Komaba, *Chem. Rev.* **2014**, *114*, 11636; b) M. D. Slater, D. Kim, E. Lee, C. S. Johnson, *Adv. Funct. Mater.* **2013**, *23*, 947.

[11] a) B. Philippe, M. Valvo, F. Lindgren, H. Rensmo, K. Edström, *Chem. Mater.* **2014**, *26*, 5028; b) X.-B. Cheng, R. Zhang, C.-Z. Zhao, F. Wei, J.-G. Zhang, Q. Zhang, *Adv. Sci.* **2016**, *3*, 1500213; c) M. A. Muñoz-Márquez, M. Zarrabeitia, E. Castillo-Martínez, A. Eguía-Barrio, T. Rojo, M. Casas-Cabanas, *ACS Appl. Mater. Interfaces* **2015**, *7*, 7801.

[12] a) G. V. Zhuang, H. Yang, B. Blizanac, P. N. Ross, *Electrochem. Solid-State Lett.* **2005**, *8*, A441; b) F. Wang, O. Borodin, M. S. Ding, M. Gobet, J. Vatamanu, X. Fan, T. Gao, N. Eidson, Y. Liang, W. Sun,

**ADVANCED
SCIENCE NEWS**

www.advancedsciencenews.com

**ADVANCED
ENERGY
MATERIALS**

www.advenergymat.de

S. Greenbaum, K. Xu, C. Wang, *Joule* **2018**, *2*, 927; c) C. Marino, A. Darwiche, N. Dupré, H. A. Wilhelm, B. Lestriez, H. Martinez, R. Dedryvère, W. Zhang, F. Ghamouss, D. Lemordant, L. Monconduit, *J. Phys. Chem. C* **2013**, *117*, 19302; d) R. L. Sacci, J. L. Bañuelos, G. M. Veith, K. C. Littrell, Y. Q. Cheng, C. U. Wildgruber, L. L. Jones, A. J. Ramirez-Cuesta, G. Rother, N. J. Dudney, *J. Phys. Chem. C* **2015**, *119*, 9816.

[13] a) G. Li, H. Li, Y. Mo, L. Chen, X. Huang, *J. Power Sources* **2002**, *104*, 190; b) Y. Ha, B. J. Tremolet de Villers, Z. Li, Y. Xu, P. Stradins, A. Zakutayev, A. Burrell, S.-D. Han, *J. Phys. Chem. Lett.* **2020**, *11*, 286; c) L. Cabo-Fernandez, D. Bresser, F. Braga, S. Passerini, L. J. Hardwick, *Batter. Supercaps* **2019**, *2*, 168; d) A. Gajan, C. Lecourt, B. E. Torres Bautista, L. Fillaud, J. Demeaux, I. T. Lucas, *ACS Energy Lett.* **2021**, *6*, 1757.

[14] a) R. M. Stöckle, Y. D. Suh, V. Deckert, R. Zenobi, *Chem. Phys. Lett.* **2000**, *318*, 131; b) H. Kim, K. M. Kosuda, R. P. Van Duyne, P. C. Stair, *Chem. Soc. Rev.* **2010**, *39*, 4820.

[15] a) T. Deckert-Gaudig, E. Kämmer, V. Deckert, *J. Biophotonics* **2012**, *5*, 215; b) W. Zhang, B. S. Yeo, T. Schmid, R. Zenobi, *J. Phys. Chem. C* **2007**, *111*, 1733.

[16] E. Bailo, V. Deckert, *Angew. Chem., Int. Ed.* **2008**, *47*, 1658.

[17] J. Nanda, G. Yang, T. Hou, D. N. Voylov, X. Li, R. E. Ruther, M. Naguib, K. Persson, G. M. Veith, A. P. Sokolov, *Joule* **2019**, *3*, 2001.

[18] B.-S. Yeo, J. Stadler, T. Schmid, R. Zenobi, W. Zhang, *Chem. Phys. Lett.* **2009**, *472*, 1.

[19] J. Stadler, T. Schmid, R. Zenobi, *Nanoscale* **2012**, *4*, 1856.

[20] a) J. S. Weaving, A. Lim, J. Millichamp, T. P. Neville, D. Ledwoch, E. Kendrick, P. F. McMillan, P. R. Shearing, C. A. Howard, D. J. L. Brett, *ACS Appl. Energy Mater.* **2020**, *3*, 7474; b) M. Anji Reddy, M. Helen, A. Groß, M. Fichtner, H. Euchner, *ACS Energy Lett.* **2018**, *3*, 2851.

[21] a) D. Mrđenović, Z.-F. Cai, Y. Pandey, G. L. Bartolomeo, R. Zenobi, N. Kumar, *Nanoscale* **2023**, *15*, 963; b) Z.-F. Cai, L.-Q. Zheng, Y. Zhang, R. Zenobi, *J. Am. Chem. Soc.* **2021**, *143*, 12380.

[22] C. Bao, B. Wang, P. Liu, H. Wu, Y. Zhou, D. Wang, H. Liu, S. Dou, *Adv. Funct. Mater.* **2020**, *30*, 2004891.

[23] a) H. Kumar, E. Detsi, D. P. Abraham, V. B. Shenoy, *Chem. Mater.* **2016**, *28*, 8930; b) Q. Liu, D. Mu, B. Wu, L. Wang, L. Gai, F. Wu, *ChemSusChem* **2017**, *10*, 786.

[24] a) S. Matsuta, T. Asada, K. Kitaura, *J. Electrochem. Soc.* **2000**, *147*, 1695; b) M. Moshkovich, Y. Gofer, D. Aurbach, *J. Electrochem. Soc.* **2001**, *148*, E155; c) G. Socrates, *Infrared and Raman Characteristic Group Frequencies: Tables and Charts*, John Wiley & Sons, Hoboken, New Jersey, US **2001**.

[25] B. L. Papke, M. A. Ratner, D. F. Shriver, *J. Phys. Chem. Solids* **1981**, *42*, 493.

[26] T. Wirth, *Angew. Chem., Int. Ed. Engl.* **1996**, *35*, 61.

[27] F. Zapata, C. García-Ruiz, *Spectrochim. Acta, Part A* **2018**, *189*, 535.

[28] R. S. Sánchez-Carrera, B. Kozinsky, *Phys. Chem. Chem. Phys.* **2014**, *16*, 24549.

[29] a) B. Han, Y. Zou, Z. Zhang, X. Yang, X. Shi, H. Meng, H. Wang, K. Xu, Y. Deng, M. Gu, *Nat. Commun.* **2021**, *12*, 3066; b) B. S. Parimalam, A. D. MacIntosh, R. Kadam, B. L. Lucht, *J. Phys. Chem. C* **2017**, *121*, 22733.

[30] a) A. Bouibes, N. Takenaka, T. Fujie, K. Kubota, S. Komaba, M. Nagaoka, *ACS Appl. Mater. Interfaces* **2018**, *10*, 28525; b) U. Purushotham, N. Takenaka, M. Nagaoka, *RSC Adv.* **2016**, *6*, 65232.

[31] H. Fu, M. Xia, R. Qi, X. Liang, M. Zhao, Z. Zhang, X. Lu, G. Cao, *J. Power Sources* **2018**, *399*, 42.

[32] a) G. Yang, X. Li, Y. Cheng, M. Wang, D. Ma, A. P. Sokolov, S. V. Kalinin, G. M. Veith, J. Nanda, *Nat. Commun.* **2021**, *12*, 578; b) Y. Sun, E. W. Chen, J. Thomas, Y. Liu, H. Tu, S. A. Boppart, *Opt. Lett.* **2020**, *45*, 3613.

[33] S. Grimme, A. Hansen, J. G. Brandenburg, C. Bannwarth, *Chem. Rev.* **2016**, *116*, 5105.